

# Two-proton radioactivity and three-body decay. V. Improved momentum distributions.

L. V. Grigorenko,<sup>1,2,3</sup> I. A. Egorova,<sup>4</sup> M. V. Zhukov,<sup>5</sup> R. J. Charity,<sup>6</sup> and K. Miernik<sup>7</sup>

<sup>1</sup>*Flerov Laboratory of Nuclear Reactions, JINR, RU-141980 Dubna, Russia*

<sup>2</sup>*Gesellschaft für Schwerionenforschung mbH, Planckstrasse 1, D-64291, Darmstadt, Germany*

<sup>3</sup>*RRC “The Kurchatov Institute”, Kurchatov sq. 1, 123182 Moscow, Russia*

<sup>4</sup>*Bogolubov Laboratory of Theoretical Physics, JINR, RU-141980 Dubna, Russia*

<sup>5</sup>*Fundamental Physics, Chalmers University of Technology, S-41296 Göteborg, Sweden*

<sup>6</sup>*Department of Chemistry, Washington University, St. Louis, Missouri 63130, USA*

<sup>7</sup>*Faculty of Physics, University of Warsaw, 00-681 Warsaw, Poland*

(Dated: June 7, 2010. File: /coul3/coul3-ex/resubmit/coul3-ex-14-resubmit.tex)

Nowadays quantum-mechanical theory allows one to reliably calculate the processes of  $2p$  radioactivity (true three-body decays) and the corresponding energy and angular correlations up to distances of the order of  $10^3$  fm. However, the precision of modern experiments has now become sufficient to indicate some deficiency of the predicted theoretical distributions. In this paper we discuss the extrapolation along the classical trajectories as a method to improve the convergence of the theoretical energy and angular correlations at very large distances (of the order of atomic distances), where only the long-range Coulomb forces are still operating. The precision of this approach is demonstrated using the “exactly” solvable semianalytical models with simplified three-body Hamiltonians. It is also demonstrated that for heavy  $2p$  emitters, the  $2p$  decay momentum distributions can be sensitive to the effect of the screening by atomic electrons. We compare theoretical results with available experimental data.

PACS numbers: 21.45.-v, 21.60.Gx, 23.50.+z

## I. INTRODUCTION

Two-proton radioactivity is the most recently discovered radioactive decay mode of nuclei and it is a very actively developing field. There were 42 years between the prediction [1] and discovery [2, 3] of  $2p$  radioactivity and, subsequently, seven years latter we have several well studied examples. A number of experiments performed in the last 2-3 years can be characterized as key for the field. In particular, correlations in the  $2p$  decays have been measured recently in  ${}^6\text{Be}$  [4],  ${}^{16}\text{Ne}$  [5],  ${}^{19}\text{Mg}$  [5, 6],  ${}^{45}\text{Fe}$  [7], and  ${}^{94}\text{Ag}$  [8] providing qualitatively new information about the  $2p$  decays. With correlation information becoming available, the  $2p$  decay studies are now turning into a field of research where precise information about structure and continuum dynamics can be obtained. It is clear that our ability to extract useful information from correlations is directly dependent on how well we understand the propagation of particles in the long-range three-body Coulomb field.

From a theoretical point of view, true two-proton decay ( $2p$  radioactivity) is an exclusively quantum-mechanical phenomenon, which has no analogue in classical physics. It is expected to be widely spread along the proton drip line with  $Z < 50$  due to peculiarities of the pairing interaction. A consistent quantum-mechanical theory of two-proton radioactivity and “democratic” three-body decays of the coulombic nuclear systems has been developed in the series of papers [9–13], which we continue here, and has been applied to different physical cases in Refs. [4, 14–17]. The complete momentum correlations for the decay of a non-aligned three-body system can

be described by two parameters. These parameters are chosen in this and our previous studies as the energy distribution parameter  $\varepsilon$  between any two of the particles and the angle  $\theta_k$  between the Jacobi momenta:

$$\begin{aligned}\varepsilon &= E_x/E_T \quad , \quad \cos(\theta_k) = (\mathbf{k}_x \cdot \mathbf{k}_y)/(k_x k_y) \quad , \quad (1) \\ E_T &= E_x + E_y = k_x^2/2M_x + k_y^2/2M_y \quad , \\ M_x &= \frac{A_1 A_2}{A_1 + A_2} M \quad , \quad M_y = \frac{(A_1 + A_2) A_3}{A_1 + A_2 + A_3} M \quad , \\ \mathbf{k}_x &= \frac{A_2 \mathbf{k}_1 - A_1 \mathbf{k}_2}{A_1 + A_2} \quad , \quad \mathbf{k}_y = \frac{A_3(\mathbf{k}_1 + \mathbf{k}_2) - (A_1 + A_2)\mathbf{k}_3}{A_1 + A_2 + A_3} \quad ,\end{aligned}$$

where  $A_i$  are mass numbers of the constituents,  $M$  is a nucleon mass, and  $E_T \equiv Q_{2p}$  is a two-proton decay energy. For two-proton emitters these parameters can be constructed in two “irreducible” Jacobi systems, called “T” and “Y”, see Fig. 1. The detailed definition of the Jacobi coordinates can be found in Ref. [4]. The complete correlation pictures for two-proton decay were, for the first time, calculated in Ref. [11]. Various aspects of the correlations between the decay products have been discussed in the theoretical works of Refs. [4, 5, 11, 12, 14].

In  ${}^6\text{Be}$  and  ${}^{45}\text{Fe}$ , the complete correlation pictures for  $2p$  decay were recently obtained experimentally [4, 7]. Moreover, the precision of these experimental results is now sufficient to show a deficiency in certain aspects of the predicted momentum distributions in the case of heavy  $2p$  emitters [17]. It was already understood in Ref. [10] that this deficiency is connected to the limited radial range of the calculations and the approximate nature of the boundary conditions employed for the treatment of the three-body Coulomb asymptotic.

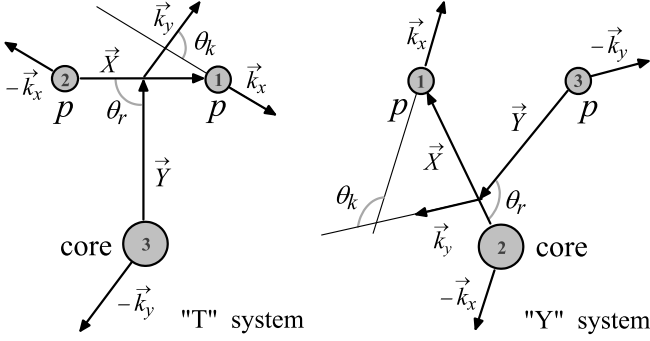


FIG. 1. Independent “T” and “Y” Jacobi systems for the core+ $N+N$  three-body system in coordinate and momentum spaces. There are “planar” cases where both the coordinates and the momenta belong to the same plane.

The classical extrapolation (CE) of momentum distributions was suggested in Ref. [11] as a simple way to estimate the possible influence of the “residual” Coulomb interaction. The basic idea is that, at small distances, particles are propagated by quantum-mechanical equations providing the three-body wave function (WF)  $\Psi_3^{(+)}$  with outgoing asymptotic. At some sufficiently large distance, the WFs are converted into “events” with definite coordinates and momenta by a Monte-Carlo (MC) procedure. However, at that time (in 2002 the  $2p$  decay of  $^{45}\text{Fe}$  was just discovered with statistics of the order of ten events [2, 3]) the need to improve this aspect of our calculations was assigned to the remote future and no detailed studies were performed. Now it seems that the development of the field has achieved the stage where the need to improve this aspect of our approach has become evident.

In this work we discuss the method of classical extrapolation in detail, demonstrate its reliability by application to exactly-solvable three-body models with a simplified Hamiltonian, and consider three “key” cases ( $^6\text{Be}$ ,  $^{19}\text{Mg}$ , and  $^{45}\text{Fe}$ ) covering a broad range of possible charges, masses, and structures for the  $2p$  emitters.

Natural system of units with  $\hbar = c = 1$  is used in this work.

## II. APPROXIMATE BOUNDARY CONDITIONS

In this section we sketch the methods used to construct the approximate boundary conditions [10] and outline existing problems. The asymptotic form of the three-body potentials in the hyperspherical harmonics (HH) method is

$$V_{K\gamma, K'\gamma'}(\rho) = \frac{U_{K\gamma, K'\gamma'}}{\rho^{3+N_{K\gamma, K'\gamma'}}} + \frac{\mathcal{L}(\mathcal{L}+1)}{\rho^2} \delta_{K\gamma, K'\gamma'} + \frac{v\eta_{K\gamma, K'\gamma'}}{\rho}, \quad (2)$$

where multiindex  $\{K\gamma\} = \{K, L, S, l_x, l_y, s_x\}$  is a complete set of quantum numbers. The matrix  $U_{K\gamma, K'\gamma'}$  arises due to contributions from the short-range nuclear forces, and  $N_{K\gamma, K'\gamma'} \geq 0$  are some integer numbers. The effective contribution of the short-range forces decreases as  $\rho^{-3}$  or faster in hyperspherical space. The diagonal centrifugal term depends on the “effective angular momentum”  $\mathcal{L} = K + 3/2$ . Coulomb pairwise potentials generate the long-range part of the hyperspherical potentials behaving as  $\rho^{-1}$ . From the technical side, the three-body Coulomb interaction causes problems due to long-range channel coupling (nonzero nondiagonal “Sommerfeld parameters”  $\eta_{K\gamma, K'\gamma'}$ ) that does not allow one to decouple the HH equations on the asymptotic. To deal with this problem, the finite-size potential matrix (in truncated hyperspherical basis) can be diagonalized with respect to the long-range term by the orthogonal transform  $\tilde{V} = A^T V A$ :

$$\tilde{V}_{K\gamma, K'\gamma'}(\rho) = \frac{\tilde{U}_{K\gamma, K'\gamma'}}{\rho^3} + \frac{C_{K\gamma, K'\gamma'}}{\rho^2} + \frac{v\eta_{K\gamma}}{\rho} \delta_{K\gamma, K'\gamma'}. \quad (3)$$

This potential includes nondiagonal “centrifugal” terms  $C_{K\gamma, K'\gamma'}$  and, to achieve the asymptotic in the diagonalized representation, we still need to go very far in  $\rho$  value, where the terms  $\sim \rho^{-2}$  become negligible compared to those with  $\sim \rho^{-1}$ . At such  $\rho$  values, the hyperradial part of the asymptotic solution with pure outgoing nature can be constructed in the form

$$\chi_{K\gamma}^{(+)}(\rho) \sim \sum_{K'\gamma'} A_{K\gamma, K'\gamma'} (G_{\mathcal{L}_0}(\eta_{K'\gamma'}, \rho) + iF_{\mathcal{L}_0}(\eta_{K'\gamma'}, \rho)),$$

$$\Psi_3^{(+)} = \rho^{-5/2} \sum_{K\gamma} \chi_{K\gamma}^{(+)}(\rho) \mathcal{J}_{K\gamma}(\Omega_5). \quad (4)$$

The functions  $F$  and  $G$  are the ordinary regular and irregular Coulomb functions. Hyperspherical harmonics  $\mathcal{J}_{K\gamma}$  are functions of the 5-dimensional “solid angle”  $\Omega_5 = \{\theta_\rho, \Omega_x, \Omega_y\}$ . Here  $\Omega_x$  and  $\Omega_y$  are ordinary solid angles of the Jacobi vectors  $\mathbf{X}$  and  $\mathbf{Y}$  [see Eq. 5] and  $\tan(\theta_\rho) = \sqrt{M_x/M_y} X/Y$ . The value  $\mathcal{L}_0$  should be larger than  $3/2$ , but otherwise does not seem to be particularly important. The WFs  $\chi^{(+)}$  provide the necessary boundary conditions for the decay problem.

The proposed boundary conditions are exact on the *truncated* hyperspherical basis at a hypersphere of *very large* radius. However on a practical level, these two requirements contradict each other: the movement further in radius requires the increase of the basis size; a larger basis size may require a larger radius. Therefore, at some point, the further radial propagation of the solution (with fixed basis size) leads to a deterioration of its quality. For  $^{45}\text{Fe}$  with the decay energy of 1.154 MeV and the basis size of  $K_{\text{max}} = 20$ , radii between 500 and 2000 fm are needed to get reasonable solutions.

There exists an analytical asymptotic of the three-body Coulomb problem (a so called “Redmond-Merkuriev” asymptotic [18, 19]), which is presumably

applicable to the true three-body decay. Practical application of this asymptotic is technically complicated and it seems that there exists a very limited experience in using such an asymptotic. At the moment we are going to avoid these complexities and to demonstrate that there exists a simple and practical way to treat the problem.

### III. EXTRAPOLATION ALONG CLASSICAL TRAJECTORIES

To perform a classical extrapolation of the quantum-mechanical result, we need to switch from a WF to classical trajectories. This should be made at some closed surface around the decay region. The procedure becomes especially simple if the whole surface is located in the region of classically allowed motion. Then the flux vectors at the surface can provide initial conditions for classical trajectories.

When using the HH coordinates there is only one variable  $\rho$ , which has a dimension of length [the 6-dimensional flux can be calculated for different  $\rho$  values, see Eq. (8)]. Therefore, it is natural in this approach to select the hypersphere with a large radius  $\rho_{\max}$  as such a surface. We will see later that tiny regions on the hypersphere with a large radius, where the pairwise distances appear to be small, do not lead to problems as the WFs in these regions are strongly suppressed. This happens due to the energy conditions defining the true  $2p$  decay: there are no long-living states in either pair of the three constituents and the strong Coulomb repulsion rapidly “expels” particles from the regions where they are close to each other.

A less evident, but important requirement is that the hyperradius  $\rho_{\max}$  is large enough that the typical distances between each pair of particles significantly exceeds the typical quantum coherence length (the “corpuscular” aspect of the problem is then far prevailing over the possible wave effects). This is a complicated issue and in each case an acceptable minimal value of  $\rho_{\max}$  should be defined by numerical experiment.

The classical trajectories formed at this hypersphere  $\rho_{\max}$  are propagated to distances  $\rho_{\text{ext}} \gg \rho_{\max}$  at which the momentum distributions are stabilized (what this exactly means we will see below). After this, the momentum distributions are reconstructed from the set of trajectories.

The pairwise distances, the Jacobi vectors, and the hyperradius are connected by the following relations

$$\begin{aligned} \mathbf{r}_{12} &= \mathbf{X}, \quad \mathbf{r}_{23} = \mathbf{Y} - c_1 \mathbf{X}, \quad \mathbf{r}_{31} = \mathbf{Y} + c_2 \mathbf{X}, \\ \rho^2 &= \frac{A_1 A_2}{A_1 + A_2} X^2 + \frac{(A_1 + A_2) A_3}{A_1 + A_2 + A_3} Y^2, \\ c_1 &= A_1 / (A_1 + A_2), \quad c_2 = A_2 / (A_1 + A_2). \end{aligned} \quad (5)$$

In the definition of the hyperradius  $\rho$ , particle  $A_3$  should be a heavy core if  $X$  and  $Y$  are defined in the “T” Jacobi system and either  $A_1$  or  $A_2$  should be a core in the “Y”

Jacobi system (see also Fig. 1 for the numbering convention).

The Newton equations of the motion for the Jacobi vectors are used to avoid the extra degrees of the freedom connected to the center-of-mass motion:

$$\begin{aligned} M_x \ddot{\mathbf{X}} &= \frac{\alpha Z_1 Z_2 \mathbf{X}}{X^3} - \frac{\alpha Z_2 Z_3 c_1 \mathbf{r}_{23}}{r_{23}^3} + \frac{\alpha Z_3 Z_1 c_2 \mathbf{r}_{31}}{r_{31}^3}, \\ M_y \ddot{\mathbf{Y}} &= \frac{\alpha Z_2 Z_3 \mathbf{r}_{23}}{r_{23}^3} + \frac{\alpha Z_3 Z_1 \mathbf{r}_{31}}{r_{31}^3}. \end{aligned} \quad (6)$$

The particular choice of the form of Eqs. (6) (“T” or “Y” Jacobi system) or the numerical precision in solving this system are not practical obstacles for getting the correct classical trajectories.

The initial conditions for these equations are defined on the hypersphere of the maximal radius achieved in the quantum-mechanical calculations:

$$\begin{aligned} \{\rho_{\max}, \Omega_\rho^{(r)}\} &\rightarrow \{\mathbf{X}(0), \mathbf{Y}(0)\}, \\ \{\mathbf{j}_x(\rho_{\max}, \Omega_\rho^{(r)}), \mathbf{j}_y(\rho_{\max}, \Omega_\rho^{(r)})\} &\rightarrow \{\dot{\mathbf{X}}(0), \dot{\mathbf{Y}}(0)\}, \end{aligned} \quad (7)$$

where  $\Omega_\rho^{(r)}$  is a randomly generated 5-dimensional hyper-angle selected by the MC procedure according to the WF density  $|\Psi_3^{(+)}|^2$  at  $\rho = \rho_{\max}$ . The flux associated with the Jacobi vectors is defined in an ordinary way:

$$\mathbf{j}_i(\rho, \Omega_\rho) = \frac{1}{M_i} \text{Im} \left[ \Psi_3^{(+)\dagger} \nabla_i \Psi_3^{(+)} \right]. \quad (8)$$

In the quantum-mechanical model of the three-body decays [9–13], the total flux  $j$  through the hypersphere  $\rho = \rho_{\max}$  define the width

$$\Gamma = j/N, \quad (9)$$

where  $N$  is normalization of the WF  $\Psi_3^{(+)}$  in the internal region. The momentum distribution (distribution density) is found as the differential of the flux  $dj/[d\varepsilon d\cos(\theta_k)]$ , see Eq. (2). In this work we compare the quantum-mechanical distributions calculated at  $\rho = \rho_{\max}$  (called below “without classical extrapolation” or “initial”) with distributions obtained by classical extrapolation to  $\rho = \rho_{\text{ext}}$  (“with classical extrapolation” or “final”).

#### A. Treatment of spins

It is implied above that the flux is averaged over the initial spin states and summed over the final spin states. Therefore the components of the WF  $\Psi_3^{(+)}$  with different total spin  $S$  can be considered as different “particles” whose contributions to the total momentum distribution should be added incoherently.

In general, three particles (or two Jacobi vectors) define a plane. Within this plane, the set of 6 equations (6) can be reduced to 4 equations. However, the momentum

vectors do not necessarily belong to this plane. It is evident that the geometry of the problem remains planar in the case of zero angular momenta of the  $X$  and  $Y$  subsystems (this situation is shown in Fig. 1). For nonzero angular momenta, some additional considerations are required.

Let us consider the flux field induced by the ordinary two-body WF with  $l \neq 0$ . For  $m = 0$ , the flux is purely radial as the angular part of the WF  $Y_{lm}$  is real (flux is an imaginary part of the gradient matrix element). For purely radial flux, the classical angular momentum associated with the particular trajectory is zero (radius and momentum vectors are collinear). This can be seen as a source of a confusion as the quantum-mechanical momentum of the WF and the classical momentum of the selected trajectory are explicitly different. The answer seems to be that the classical characteristic of the trajectory should be related to average corresponding characteristic of the WF.

In the three-body case, the ground-state WFs typically have two major components: the dominating  $L = 0$  component and an “admixture”  $L = 1$  component. We imply here that a spin-zero core is considered; the two spin 1/2 protons can then be coupled into the total spins  $S = 0$  or  $S = 1$ . The  $L = 0$  component of the WF is formed by terms with angular momenta in the subsystem  $l_x = l_y$ . It is easy to check that the angular part of this WF  $[Y_{l_x} \otimes Y_{l_x}]_{00}$  is real and thus the classical angular momentum associated with any trajectory induced by this WF is zero. The decay in this case is *planar* (we mean that for any generated event, a plane can be selected in which the coordinate vectors and the momentum vectors of all three particles are simultaneously located).

It is more complicated when the  $L = 1$  component is considered. It is possible to demonstrate that for the  $[Y_{l_x} \otimes Y_{l_x}]_{1M}$  component of the WF with  $M = 0$ , the configuration of the classical momenta is planar, while for  $M \neq 0$ , the planes formed by the three radii and by the three momenta does not coincide. However according to the Wigner-Eckart theorem, in order to define the observables it is sufficient to calculate the matrix elements for only one projection and the rest are reconstructed by the angular momentum algebra. Therefore, it seems sufficient to calculate the distributions for  $M = 0$  (planar case calculations are especially simple), while the distributions for  $M = \pm 1$  should be the same.

#### IV. TEST CASES OF SOLVABLE SEMIANALYTICAL MODELS

In Ref. [12], a semianalytical model was developed which allows one to treat exactly the asymptotic behaviour of the three-body Coulomb WF for certain simplified three-body Hamiltonians. The basic idea of the model is that instead of the real three-body Hamiltonian

$$H_3 = T_x + T_y + V_{12}(\mathbf{r}_{12}) + V_{23}(\mathbf{r}_{23}) + V_{31}(\mathbf{r}_{31}), \quad (10)$$

we use the model Hamiltonian depending not on pairwise vectors  $\mathbf{r}_{ij}$  but on the Jacobi vectors  $\mathbf{X}$  and  $\mathbf{Y}$

$$H_3 = T_x + T_y + V_x(\mathbf{X}) + V_y(\mathbf{Y}) + V_3(\rho), \quad (11)$$

The three-body potential  $V_3(\rho)$  is used in this work has the Woods-Saxon form

$$V_3(\rho) = V_3^0 (1 + \exp[(\rho - \rho_0)/a_\rho])^{-1}, \quad (12)$$

$$\rho_0 = \sqrt{2} \, 1.2 (A_{\text{core}} + 1)^{1/3}, \quad (13)$$

with a small value of the diffuseness parameter  $a_\rho = 0.4$  fm. The depth  $V_3^0$  of this potential is used to control the decay energy of the system. The potentials  $V_x$  and  $V_y$  contains the nuclear and the Coulomb contributions. The Coulomb potential of the homogeneously-charged sphere with a radius  $r_{\text{sph}}$  is used. The nuclear parts are described by Woods-Saxon formfactors with radii taken from systematics.

In conjunction with this simplified Hamiltonian of Eq. (11), we can introduce an auxiliary Hamiltonian

$$\bar{H}_3 = T_x + T_y + V_x(\mathbf{X}_{12}) + V_y(\mathbf{Y}_{23}), \quad (14)$$

for which the Green’s function can be constructed in an analytical form

$$G_{E_T}^{(+)}(\mathbf{X}\mathbf{Y}, \mathbf{X}'\mathbf{Y}') = \frac{1}{2\pi i} \int_{-\infty}^{\infty} dE_x G_{E_x}^{(+)}(\mathbf{X}, \mathbf{X}') G_{E_y}^{(+)}(\mathbf{Y}, \mathbf{Y}'), \quad (15)$$

where  $E_T$  is the total decay energy,  $E_x = \varepsilon E_T$ , and  $E_y = (1 - \varepsilon)E_T$  are the energies of the Jacobi subsystems. The above two-body Green’s functions correspond to the  $X$  and  $Y$  subhamiltonians of  $\bar{H}_3$ . Based on Eq. (15), the width and the energy distribution for the system defined by the Hamiltonian of Eq. (11) can be obtained from

$$\frac{d\Gamma}{d\varepsilon} = \frac{dj}{d\varepsilon} = \frac{8}{\pi} E_T \frac{M_x M_y}{k_x(\varepsilon) k_y(\varepsilon)} |A(\varepsilon)|^2, \quad (16)$$

where  $dj/d\varepsilon$  is a differential of the flux at the asymptotic. For a particular set of quantum numbers  $l_x, l_y$ , the amplitudes  $A(\varepsilon)$  are defined via the scattering eigenfunctions  $\varphi_{l_i}$  of subhamiltonians of (14):

$$A(\varepsilon) = \int_0^\infty dX \int_0^\infty dY \varphi_{l_x}(k_x(\varepsilon)X) \varphi_{l_y}(k_y(\varepsilon)Y) \times V_3(\rho) \varphi_{Ll_x l_y S}(X, Y). \quad (17)$$

The WF  $\varphi_{Ll_x l_y S}(X, Y)$  is the quasistationary eigenfunction of (11), deduced in a three-body hyperspherical approach. The particular choice of the boundary conditions for this WF (for sufficiently large radius of the “box”) is not important in the model. The quasistationary WF is normalized to unity in the internal region, which gives the identity  $d\Gamma/d\varepsilon \equiv dj/d\varepsilon$  in Eq. (16).

The results obtained in this model are quoted below as “exact” as they do not suffer from any convergence/stability issues. In Sections IV A and IV B, we will use models with different simplified Hamiltonians to test the classical-extrapolation procedure in the case of the  $^{19}\text{Mg}$ -ground-state (g.s.) decay and only after that we will turn to more realistic situations.

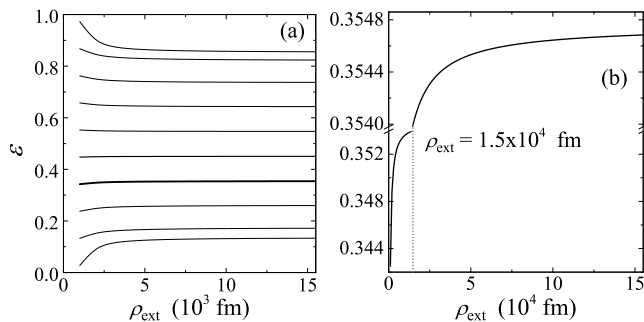


FIG. 2. Classical trajectories for  $^{19}\text{Mg}$  in a direct decay model ( $\rho_{\text{max}} = 1000$  fm,  $E_T = 0.75$  MeV). Panel (b) shows one selected trajectory on a large scale. The dotted line in panel (b) corresponds to the scale of the panel (a).

### A. Direct-decay model

The Hamiltonian of Eq. (11) constructed in the “Y” Jacobi system corresponds to some physically well justified approximations. Namely, (i) we neglect the proton-proton interaction and (ii) for one of the core-proton potentials we use the Jacobi  $Y$  variable instead of the relative distance. The later assumption becomes correct in the limit of an infinitely-heavy core and thus should work well for heavy  $2p$  emitters.

Let us consider the “Y” system, where the subsystem {core+proton} is taken as an effective particle lying on the  $X$  coordinate as shown Fig. 1:

$$V^{\text{coul}} = \frac{\alpha Z_1 Z_2}{X} + \frac{\alpha(Z_1 + Z_2)Z_3}{Y}. \quad (18)$$

In this case, we include both pairwise interactions  $V_x^{\text{nucl}}$  and  $V_y^{\text{nucl}}$ . The system with such a composition of potentials in the “Y” system was labeled as “Two final-state interactions” in Ref. [12].

For the  $^{19}\text{Mg}$  g.s., we assume the pure  $d$ -wave structure  $l_x = l_y = 2$  in this model. The nuclear Woods-Saxon potential was used with the radius

$$r_0 = 1.2 (A + 1)^{1/3} \quad (19)$$

and diffuseness  $a = 0.65$  fm. The depth of the potentials was adjusted to give an energy of 1.3 MeV for the ground-state resonance in  $^{18}\text{Na}$  [6] and the Coulomb potential of the charged sphere with radius

$$r_{\text{sph}} = \sqrt{\frac{5}{3} (1.2A^{1/3})^2 + 0.8^2} \quad (20)$$

was used. In the above expressions, one should substituted  $A = A_2$  in the  $X$  subsystem and  $A = A_2 + 1$  in the  $Y$  subsystem. In this model, we obtained the half-life of  $T_{1/2} = 58$  ps (corresponding to  $\Gamma = 7.9 \times 10^{-11}$  MeV) which is in qualitative agreement with the experimental value for  $^{19}\text{Mg}$  ( $T_{1/2} = 4$  ps [6]).

The radial convergence of the energy distribution  $\varepsilon$  in this model for some classical trajectories is illustrated in

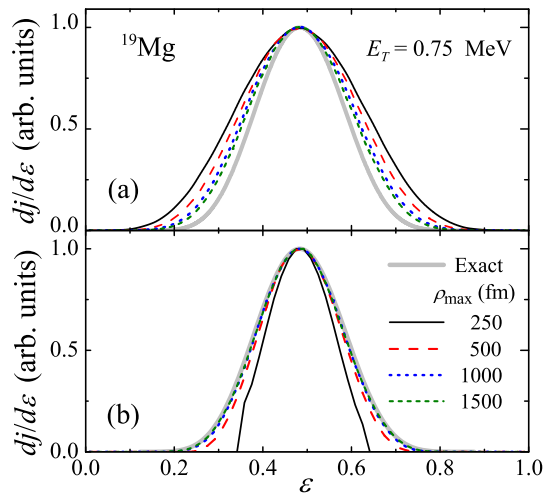


FIG. 3. (Color online) Energy distribution for  $^{19}\text{Mg}$  with different  $\rho_{\text{max}}$  values without (upper panel) and with (lower panel) classical extrapolation in the direct decay model. The calculations are performed with  $E_T = 0.75$  MeV,  $K_{\text{max}} = 20$ , and lower panel with  $\rho_{\text{ext}} = 40000$  fm. Gray curve shows the exact result of Eq. (16) (the same for both panels).

Fig. 2. The trend of the CE is to make the energy distribution narrower. The visual stability of the distributions is achieved at distances of about  $\rho_{\text{ext}} \sim 7000$  fm [Fig. 2(a)]. On a larger scale, a certain drift of the trajectories can be seen up to much larger distances [Fig. 2(b)].

The effect of the CE on the energy distributions is demonstrated in Fig. 3. The energy distributions have a characteristic bell shape. The upper panel shows the energy distributions calculated with the quantum-mechanical three-body model [12] for different  $\rho_{\text{max}}$  values. The calculated result tends towards the “exact” result of Eq. (16), shown by the gray curves. However, this convergence is very slow and some discrepancy remains even for the largest available  $\rho_{\text{max}}$ . The lower panel shows the distributions obtained with the classical extrapolation. These distributions are clearly wrong for  $\rho_{\text{max}} \lesssim 500$  fm. However for larger  $\rho_{\text{max}}$ , they stabilize and reproduce the results of the solvable model [Eq. (16)] within the width of the curve.

### B. “Diproton” model

The word “diproton” in parenthesis is the name of this model as it is different from the diproton model typically used in the literature. The diproton correlation in our model is not introduced statically (which means “by hand”) but is treated dynamically. In Ref. [12], we have demonstrated that when introduced appropriately for the configurations with lowest possible angular momenta in the subsystems, the diproton model can provide only a very small value for the  $2p$  width. For decays of the higher- $l$  configurations, like  $[p^2]$  or  $[d^2]$  for  $0^+$  states,

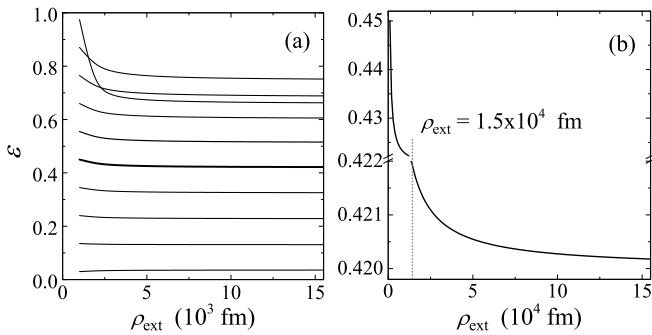


FIG. 4. Classical trajectories for  $^{19}\text{Mg}$  in the “diproton” model ( $\rho_{\text{max}} = 1000$  fm,  $E_T = 0.75$  MeV). Panel (b) shows one selected trajectory on a large scale. The dotted line in panel (b) corresponds to the scale of panel (a).

this model overestimates the width. Therefore, it is not applicable in practice, in contrast to widespread beliefs.

In this work we apply the diproton model, not for realistic estimates, but for testing purposes. The diproton model gives very sharp energy distributions focused at small  $p$ - $p$  energies. So, we use it to determine whether the CE procedure works for conditions of strong kinematical focusing.

In the diproton model, Eqs. (11)–(17) are used in the “T” system, where the core  $\{A_3, Z_3\}$  interacts with the two protons as if they were an effective particle  $\{A_1 + A_2, Z_1 + Z_2\}$ . The Coulomb potential of the simplified Hamiltonian can be written in the form

$$V^{\text{coul}} = \frac{\alpha Z_1 Z_2}{X} + \frac{\alpha (Z_1 + Z_2) Z_{\text{core}}}{Y}. \quad (21)$$

Note, that this is a model with only one nuclear pairwise interaction  $V_x^{\text{nuc}}(X)$  in the  $p$ - $p$  channel (the second interaction can be put to zero) and therefore the model is called “One final-state interaction” in Ref. [12]. The proton-proton nuclear potential for an  $s$ -wave is taken as a single Gaussian

$$V(r) = V_0 \exp[-(r/r_0)^2], \quad (22)$$

with  $V_0 = -31$  MeV and  $r_0 = 1.8$  fm reproducing the low-energy  $s = 0$  nucleon-nucleon phase shifts. The Coulomb potential of the charged sphere with radius

$$r_{\text{sph}} = \sqrt{\frac{5}{3} \left(1.2 A_{\text{core}}^{1/3}\right)^2 + \frac{5}{3} \left(1.2 \times 2^{1/3}\right)^2} \quad (23)$$

is used in the  $Y$  coordinate. The half-life of  $^{19}\text{Mg}$  obtained in this model is  $T_{1/2} = 0.39$  ps (corresponding to  $\Gamma = 1.2 \times 10^{-9}$  MeV).

The radial convergence of the energy  $\varepsilon$  in this model for some classical trajectories is illustrated in Fig. 4. The trend of the CE is for the trajectories to drift towards the more narrow “diproton” peak in the energy spectrum. The convergence trend is analogous to the direct-decay model with several thousand fm required for a reasonable stabilization and more than a hundred thousand fm required for complete stability.

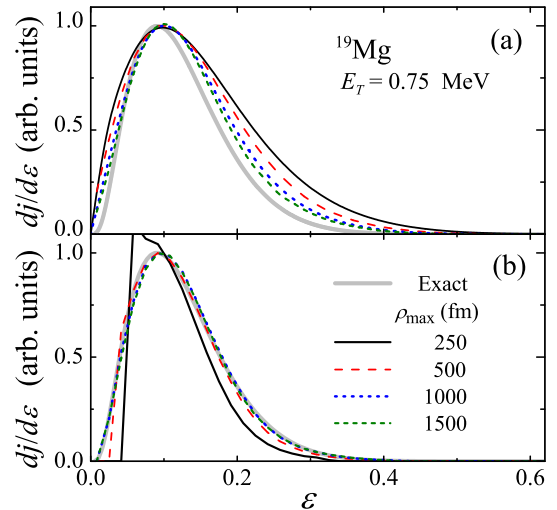


FIG. 5. (Color online) Energy distributions in  $^{19}\text{Mg}$  for the “diproton” model without (upper panel) and with (lower panel) classical extrapolation. Calculation results are shown for different  $\rho_{\text{max}}$  values. The calculations are performed with  $E_T = 0.75$  MeV,  $K_{\text{max}} = 14$  and for lower panel with  $\rho_{\text{ext}} = 10^5$  fm. Gray curves show the “exact” result of Eq. (16) (the same for both panels).

The effect of the CE on the energy distribution is demonstrated in Fig. 5. The case appears to be completely analogous to the direct-decay model. The upper panel shows the energy distributions calculated within our three-body hyperspherical quantum-mechanical approach for different  $\rho_{\text{max}}$  values. The quantum-mechanical results tend towards the “exact” result (16), but only very slowly. The distributions provided by the classical extrapolation (see the lower panel in Fig. 5) contain artifacts for  $\rho_{\text{max}} \lesssim 500$  fm, but for larger  $\rho_{\text{max}}$ , they stabilize and reproduce the result of the solvable model Eq. (16) within the width of the curve.

### C. Brief conclusions

Before we continue studies of realistic cases, let us outline what we can conclude on the basis of the exactly-solvable models with simplified Hamiltonians.

- (i) The quantum-mechanical calculations performed for  $\rho_{\text{max}}$  of a few thousand fm give energy distributions which have visible deviations from the “exact” results obtained in the semianalytical model. The extrapolated distributions practically coincide with the “exact” ones.
- (ii) The CE provides decent results only if the starting point for the extrapolation is sufficiently large. Pragmatically, this means that the classical trajectories in the kinematical space  $\{\varepsilon, \cos(\theta_k)\}$  should be quite short. The same should be true in the

conjugated coordinate space. It can be expected that the criterion of a successful transition from quantum to classical calculation is that the classical variation of a position in some space should be smaller than corresponding coherence length.

- (iii) Distances of tens of thousands of fm's are needed to achieve complete stabilization of classical trajectories in practice. Some very minor drift continues after that, reflecting the long-range nature of the Coulomb interaction. However, it is evident that distances of  $\sim 10^5$  fm are already atomic scale distances and the nuclear Coulomb effects should be suppressed for larger distances due to some form of electron screening.

Near perfect convergence of the extrapolated distributions to those calculated in the exact semianalytical models with the simplified Hamiltonians is *not a proof* that the procedure should work perfectly in the case of a complete three-body Hamiltonian. However, it is very encouraging and we can expect that the quality of convergence in the realistic case will be very similar, as the kinematical conditions for the decay in the simplified models are chosen to be the same as in the realistic cases.

## V. REALISTIC THREE-BODY CASES

For the models with simplified Hamiltonians, we demonstrated only the energy distributions (angular distributions are trivial) and only in one Jacobi system (the one in which the particular semianalytical model is formulated). Conversion of the distribution into the other Jacobi system in this case does not provide an additional information. For realistic calculations we will demonstrate complete correlation pictures (on kinematical  $\{\varepsilon, \cos(\theta_k)\}$  plane) simultaneously in both “T” and “Y” Jacobi systems. It should be understood that correlation pictures in “T” and “Y” Jacobi systems are just different representations of the same physical phenomenon. Conversion between these distributions is trivial. Nevertheless, we systematically demonstrate both of them simultaneously as each representation allows one to reveal different aspects of the correlations (see Ref. [17] as example).

### A. Decay of the ${}^6\text{Be}$

Very precise complete correlation data have recently been obtained for  ${}^6\text{Be}$  in Ref. [4]. The detailed theoretical studies of  $2p$  decay of the  ${}^6\text{Be}$   $0^+$  ground state have been carried out in this work and compared to the experimental data. The dynamical range of around  $\rho_{\text{max}} = 1000$  fm used in these calculations was estimated in Ref. [4] as sufficient for essentially complete convergence of the momentum distributions. A very nice agreement between theory and experiment was found in this work. We would

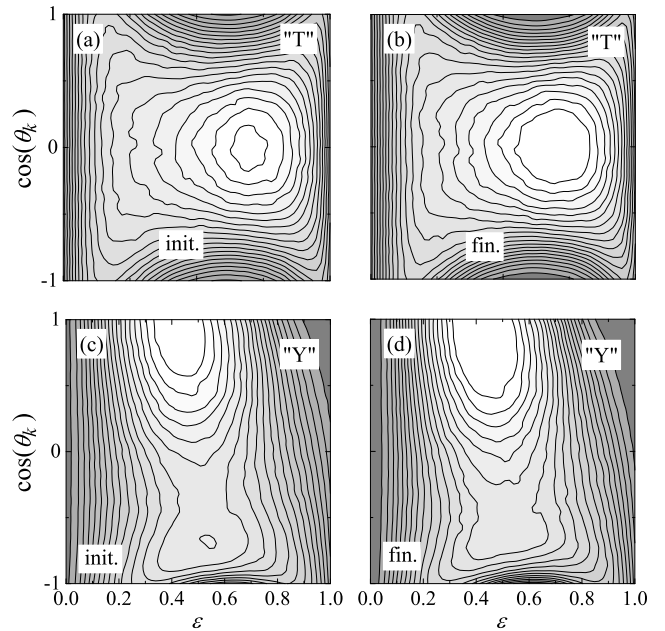


FIG. 6. Contour maps of the distribution density on the kinematical plane  $\{\varepsilon, \cos(\theta_k)\}$  for  ${}^6\text{Be}$  in “T” (upper row) and “Y” (lower row) Jacobi coordinate systems without (left panels, “init.”) and with (right panels, “fin.”) classical extrapolation.

like to check here whether the conclusions obtained in Ref. [4] can be influenced by a more careful treatment of the momentum distributions.

The classical trajectories for  ${}^6\text{Be}$  in the kinematical space are all very short. Only the trajectories corresponding to small initial inter-particle distances [ $\varepsilon \sim 0.5$ ,  $\cos(\theta_k) \sim \pm 1$  in “T” system] have noticeable lengths. The complete correlation densities without and with extrapolation are shown in Fig. 6 (this is the calculation with potential set P2 from Ref. [4], which was found to be the optimal choice in that work). The distributions are very similar except for the aforementioned regions of small initial inter-particle distances. A closer look at these regions is provided in the inclusive distributions in Fig. 7. The maximal effect can be found at small  $\varepsilon$  values (corresponding to the lowest relative-energy motion between two of the particles) or for the angular distribution in the middle energy bins around  $\cos(\theta_k) \sim \pm 1$  (in the “T” system) and  $\cos(\theta_k) \sim -1$  (in the “Y” system).

Comparisons with experimental angular distributions [4] are shown in Fig. 8. The theoretical curves here are visibly distorted (relative to Fig. 7) as the comparison is based on the full MC simulation of the experimental setup [4], which takes into account the effects of the experimental bias and resolution. The effect of the classical extrapolation is at the limit of the experimental sensitivity. Quantitatively the  $\chi^2/\nu$  values without extrapolation are 1.17 (in the “T” system) and 1.14 (in the “Y” system). The same values with extrapolation are found as 1.20 and 1.16, respectively. This is a little worse, but



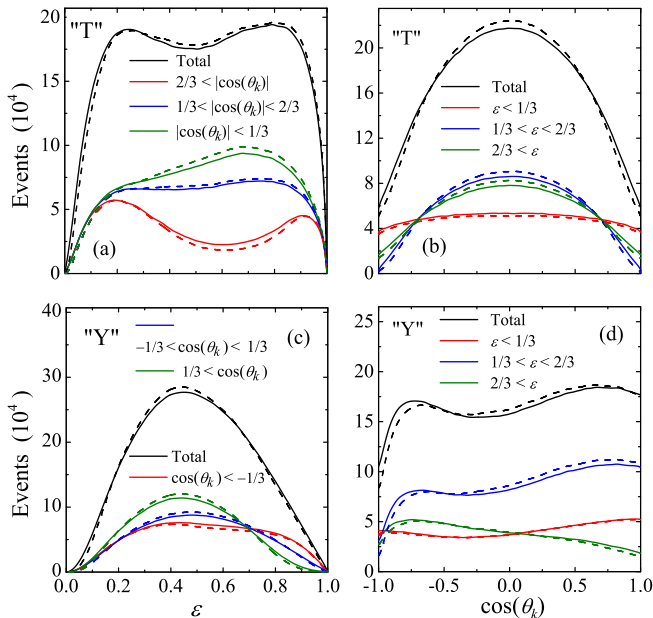


FIG. 7. (Color online) Inclusive energy and angular distributions for  ${}^6\text{Be}$  in “T” (upper row) and “Y” (lower row) Jacobi coordinate systems without (solid curves) and with (dashed curves) classical extrapolation. Black lines show the total distribution and the color coded lines show the inclusive distributions for certain energy and angular bins (described in the legends).

not really significant. On the other hand, there seems to be a minor improvement of the agreement for the parts of the middle energy bins mentioned in the previous paragraph.

The properties of the  ${}^6\text{Be}$  continuum are actively investigated now. The new higher precision experiments have been performed recently at NSCL (Michigan State University) and at Flerov laboratory (JINR, Dubna, Russia). The expected precision of these experiments would make the improvement of the theoretical distributions introduced in this work a necessary part of the data interpretation.

### B. Decay of the ${}^{19}\text{Mg}$

A systematic view of the classical trajectories on the kinematical plane for  ${}^{19}\text{Mg}$  is given in Fig. 9. The “lengths” of the trajectories here are significant: typically around 10 – 15% of the kinematical variable range thus making the CE procedure necessary for quantitative calculations of the momentum distributions.

An improvement of the momentum distribution due to classical extrapolation is demonstrated in Fig. 10 for the complete momentum distributions and in Fig. 11 for the inclusive ones. It can be seen that the angular distributions in the “T” and the energy distributions in the “Y” Jacobi systems are the most sensitive to the extrap-

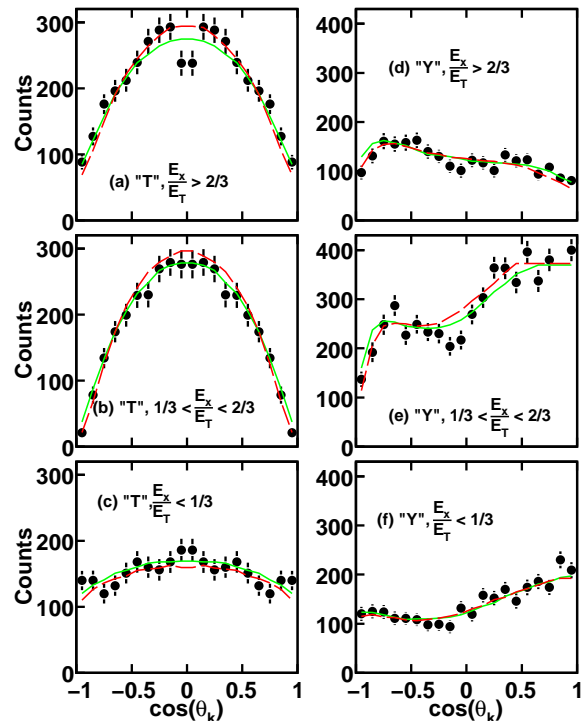


FIG. 8. (Color online) Comparison of experimental (data points [4]) and predicted (curves)  $\cos(\theta_k)$  distributions in the “T” (left) and “Y” (right) Jacobi systems for the indicated gates on  $\varepsilon = E_x/E_T$  parameter. The solid (green) and dashed (red) curves correspond to the three-body calculations without and with classical extrapolation. The effect of the detector bias and resolution is included.

olation. The effect of the extrapolation on the distributions in certain energy and angular bins can be very large. The energy distribution in the “T” system is only slightly modified by the CE, but it is interesting to note that for very small  $\varepsilon$  values (where  $p$ - $p$  Coulomb interaction is expected to be most active) the extrapolated distribution is visibly suppressed.

Unfortunately the available experimental data on the momentum distributions in  ${}^{19}\text{Mg}$  [6] do not provide complete distributions, but provide distributions projected on a plane (perpendicular to the incident beam axis). Such distributions integrated over one variable have lost some information and can be more complicated to interpret.

### C. Decay of the ${}^{45}\text{Fe}$

The  ${}^{45}\text{Fe}$  nucleus is the heaviest  $2p$  emitter studied so far and the effect of the CE is the largest, see Fig. 12.

Radial stabilization of the values  $\varepsilon$  and  $\cos(\theta_k)$  for one selected trajectory is demonstrated in Fig. 13 (this trajectory is shown in the gray ellipse in Fig. 12). The trajectories are well “converged” by about  $(3 - 4) \times 10^4$  fm but some drift continues up to much larger  $\rho$  values. In real



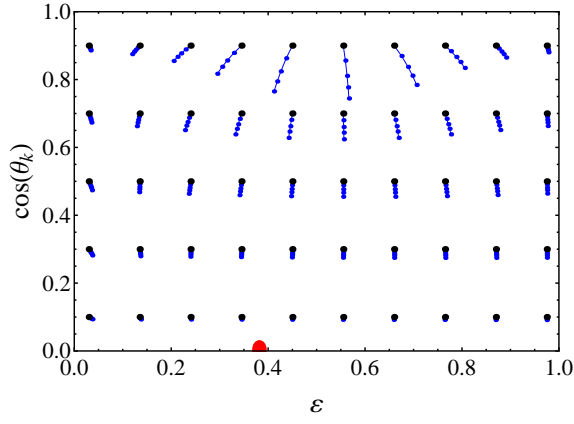


FIG. 9. (Color online) Classical trajectories on the kinematical plane  $\{\varepsilon, \cos(\theta_k)\}$  for  $^{19}\text{Mg}$  in the Jacobi “T” system. Starting points (larger black dots) correspond to  $\rho_{\text{max}} = 1000$  fm. Dots in the curves correspond to  $\rho_{\text{ext}}$  equal 1300, 2000, 3500, and  $10^5$  fm. The red dot at the axis  $\cos(\theta_k) = 0$  corresponds to a stationary point, see the discussion in Sec. VIC.

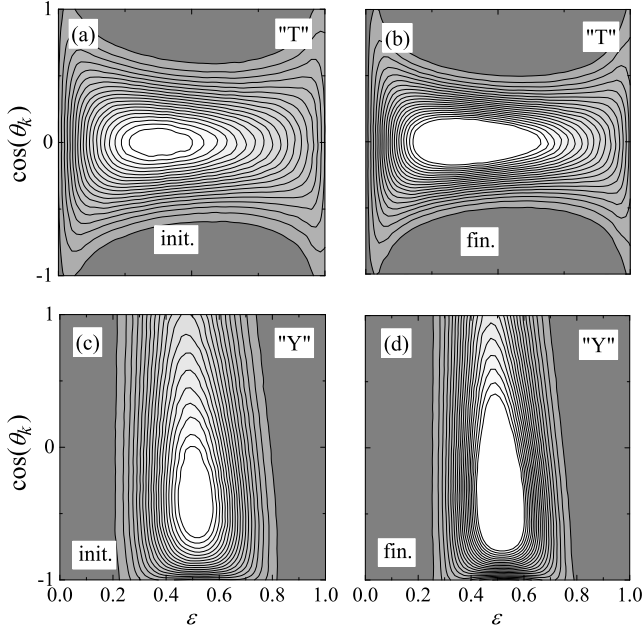


FIG. 10. Contour maps of the distribution density on the kinematical plane  $\{\varepsilon, \cos(\theta_k)\}$  for  $^{19}\text{Mg}$  in “T” (upper row) and “Y” (lower row) Jacobi coordinate systems without (left panels, “init.”) and with (right panels, “fin.”) classical extrapolation.

experimental situations, this slow drift can be suppressed by electron screening which is discussed separately in Sec. VIB.

The improvement of the momentum distributions due to the classical extrapolation for  $^{45}\text{Fe}$  is demonstrated in Fig. 14 for the complete momentum distributions and in Fig. 15 for the inclusive ones. The most impressive modifications are for the  $\varepsilon$  distribution in the “Y” system and

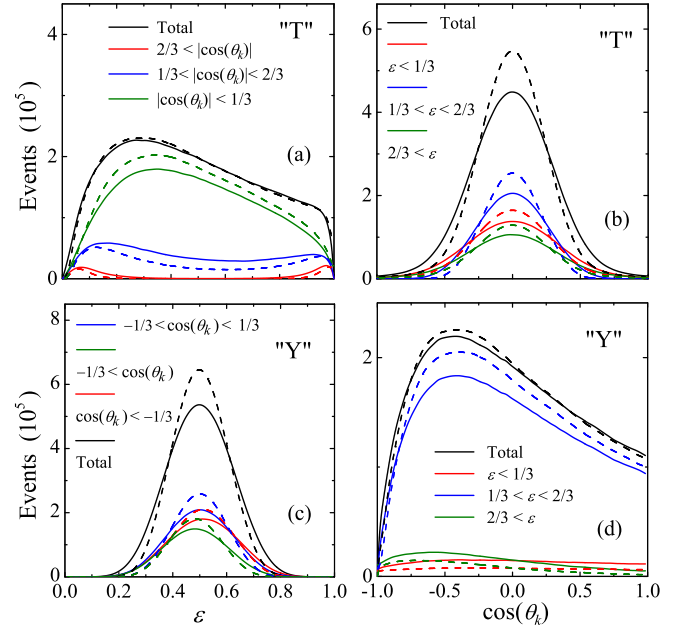


FIG. 11. (Color online) Inclusive energy and angular distributions for  $^{19}\text{Mg}$  in “T” (upper row) and “Y” (lower row) Jacobi coordinate systems without (solid curves) and with (dashed curves) classical extrapolation. Black lines show the total distribution and the color coded lines show the inclusive distributions for certain energy and angular bins (described in the legends).

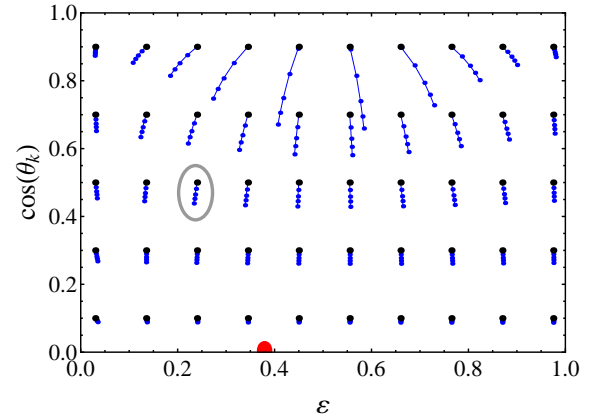


FIG. 12. (Color online) Classical trajectories on the kinematical plane  $\{\varepsilon, \cos(\theta_k)\}$  for  $^{45}\text{Fe}$  in the Jacobi “T” system,  $E_T = 1.154$  MeV. Starting points (larger black dots) correspond to  $\rho_{\text{max}} = 1000$  fm. Dots in the curves correspond to  $\rho_{\text{ext}}$  equal 1400, 2200, 4000, and  $10^5$  fm. The red dot at the axis  $\cos(\theta_k) = 0$  corresponds to a stationary point, see the discussion in Sec. VIC.

for the  $\cos(\theta_k)$  distribution in the “T” system. As far as these distributions have bell shapes, centered at (or close to) the center of the kinematical range, we can characterize them in terms of the full width at half maximum (FWHM). Classical extrapolation decreases this value by about 30% for  $\cos(\theta_k)$  in “T” system and by about 10%

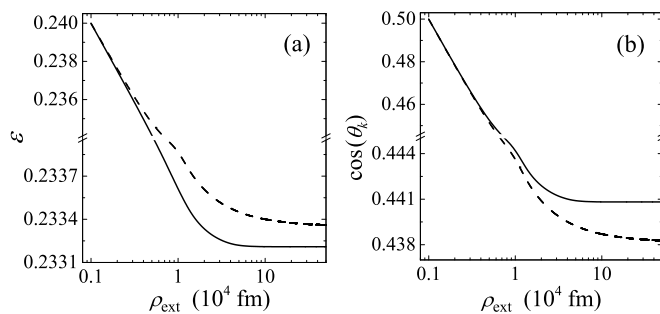


FIG. 13. Radial stabilization of the values  $\varepsilon$  [panel (a)] and  $\cos(\theta_k)$  [panel (b)] with  $\rho$  in the case of screened Coulomb potential (solid curves) and in the case of nuclear Coulomb potential only (dashed curves) for one selected trajectory in  $^{45}\text{Fe}$  (see Fig. 12).  $E_T = 1.154$  MeV,  $\rho_{\text{max}} = 1000$  fm.

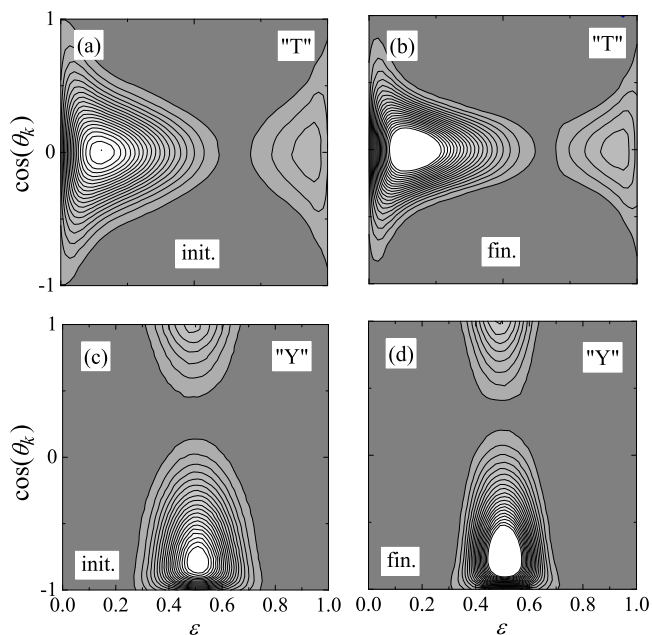


FIG. 14. Contour maps of the distribution density on the kinematical plane  $\{\varepsilon, \cos(\theta_k)\}$  for  $^{45}\text{Fe}$  in 'T' (upper row) and 'Y' (lower row) Jacobi coordinate systems without (left panels, 'init.') and with (right panels, 'fin.') classical extrapolation.

for  $\varepsilon$  in 'Y' system. This effect is sufficiently large to be already observable at the current level of the experimental precision.

The experimental distribution for  $^{45}\text{Fe}$  [7] has quite low statistics (150 events) and therefore it is far from being smooth, see Fig. 16 (a). To make a visual comparison with theoretical calculations possible, we produce a "smooth" representation of this data based on the experimental uncertainties. The raw experimental data measured in [7] by an optical time projection chamber consists of the energies and the polar angles of the two protons and the azimuthal angle between the projections of the two protons' momenta on the cathode plane of the

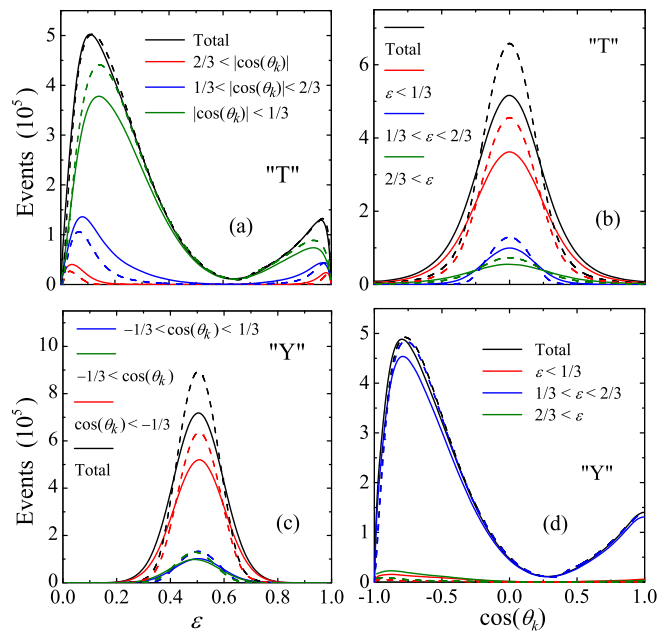


FIG. 15. (Color online) Inclusive energy and angular distributions for  $^{45}\text{Fe}$  in 'T' (left column) and 'Y' (right column) Jacobi coordinate systems without (solid curves) and with (dashed curves) classical extrapolation. Black lines show the total distribution and the color coded lines show the inclusive distributions for certain energy and angular bins (described in the legends).

chamber. Each parameter for each event has a value (and its uncertainty) defined individually by a complex iterative fitting procedure. Instead of each event, we generate an event distribution based on the stochastic Gaussian variation of each parameter within its uncertainty range. So instead of one point in the kinematic space we get a kind of a "probability cloud". The result of this procedure is shown in Fig. 16 (b). This procedure is not a cure for small statistics, but for small statistics and large experimental uncertainties we think it is a preferable presentation as it incorporates information about the distortions caused by the measurement procedure in a consistent and visible way.

The experimental data are compared with inclusive theoretical distributions sensitive to the classical extrapolation in Fig. 17. In this plot, theoretical results were treated by the procedure which is maximally close to the experimental treatment of the data: (i) for the "theoretical event" the nearest experimental event in the space of parameters  $\{E_{p1}, E_{p2}, \theta_1, \theta_2, |\phi_2 - \phi_1|\}$  was defined, (ii) spherical coordinates for protons from the "theoretical event" were distributed according to the errors of the nearest experimental event, (iii) the momentum of the core was reconstructed and the total energy of the "distorted" theoretical event was renormalized to correspond exactly to the experimental one, and (iv) a new location in the kinematical plane  $\{\varepsilon, \cos(\theta_k)\}$  was defined. The effect of the experimental resolution is a roughly 25%

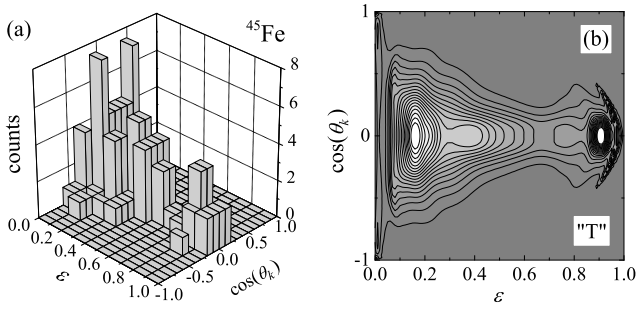


FIG. 16. Experimental distribution density in  $^{45}\text{Fe}$  in “T” Jacobi system. Original distribution from [7] is shown in the panel (a) as a histogram. “Smooth” version of this distribution taking into account experimental errors is shown in the panel (b) as a contour plot.

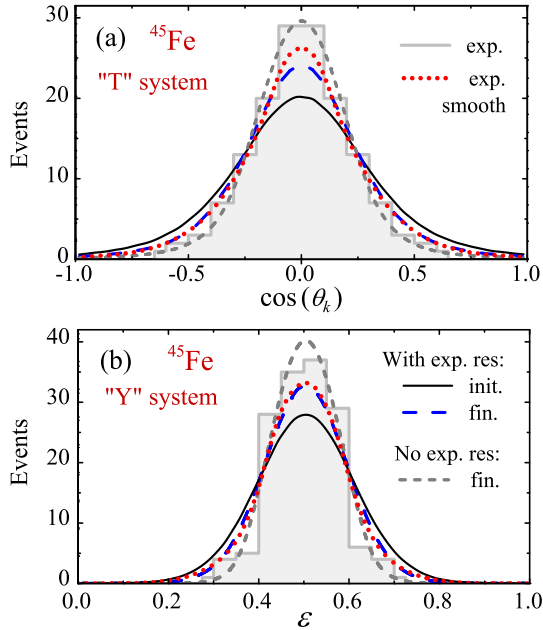


FIG. 17. (Color online) Inclusive angular (a) and energy (b) distributions for  $^{45}\text{Fe}$  in “T” and “Y” Jacobi coordinate systems without (“init.”) and with (“fin.”) classical extrapolation compared to the experimental data. The results with experimental resolution of [7] and without it are explained in legends, which are the same for both panels.

increase of FWHM for the  $\epsilon$  distribution and an 18% increase of FWHM for the  $\cos(\theta_k)$  distribution (see Fig. 17). It can also be seen in Fig. 17 that the theoretical results with classical extrapolation are in quantitative agreement with the experiment, while without CE they are not completely consistent with the data. So, we have appreciable experimental evidence that the long-range treatment of the momentum distributions (namely CE) is necessary for heavy  $2p$  emitters.

## VI. DISCUSSION

### A. Classical motion

It is important to note that large hyperradii are used to start the classical extrapolation procedure. Specifically for true  $2p$  decay with such large hyperradii, practically the whole WF resides is in the classically allowed region (probability to find the system in the classically forbidden region is very small). For example, for the  $^{45}\text{Fe}$  calculation with hyperradius  $\rho_{\text{max}} = 1000$  fm and MC generation of  $10^7$  events it is typical that not a single event is generated which is situated in the classically forbidden region. This fact confirms the validity of the choice of a hypersphere as the surface at which the switching from quantum-mechanical to classical methods is performed.

### B. Electron screening

The discussion of the  $^{45}\text{Fe}$  case can provide an illustrative example here. So far, the decay process of  $^{45}\text{Fe}$  with the half-life of 2.6 ms [7] was measured in gas (or solid state) detectors. This means that at the moment of decay,  $^{45}\text{Fe}$  has completely recovered electron shell. The Bohr radius for  $^{45}\text{Fe}$  is

$$a_0 = \frac{1}{m_e \alpha Z} = 2035 \text{ fm}, \quad (24)$$

where  $Z = \sum_i Z_i$  is total charge of  $^{45}\text{Fe}$ . Therefore, we can expect that the screening effect of the inner most electrons becomes observable at about 2000 fm. Classical trajectories for  $^{45}\text{Fe}$  in kinematical space are well stabilized by  $10^5$  fm, but there is a minor drift up to much larger distances. It is clear that some effect of the electron screening on the momentum distributions can be expected.

The binding energy of all electrons estimated as independent particles is  $\sum_i m_e (Z/2n_i \alpha)^2$  ( $n_i$  is a principal quantum number of the shell), which gives 52.3 and 47.8 keV for  $^{45}\text{Fe}$  and  $^{43}\text{Cr}$ , respectively. So, when  $^{45}\text{Fe}$  emits two protons at least two electrons should be ejected carrying away 4.5 keV of energy. The estimated velocities of protons with energies around 0.5 MeV and electrons with energies around 1 keV are 0.033 and 0.063. These velocities are comparable, which means that the  $2p$  decay of atomic  $^{45}\text{Fe}$  would be accompanied by a strong reconstruction of atomic structures having the same timescale. It is reasonable therefore to make estimates of a screening with the  $^{45}\text{Fe}$  electron density, but only for 24 electrons. This will somehow account for the effect of the electron shell disintegration during the  $2p$  decay of  $^{45}\text{Fe}$  and provide a nuclear plus atomic Coulomb potential tending to zero at infinity.

The electron density used for the screening calculations and the potentials obtained are shown in Fig. 18. One can see already that at 2000 fm, the full  $(V_{\text{coul}}^{\text{nuc}} + V_{\text{coul}}^{\text{el}})$

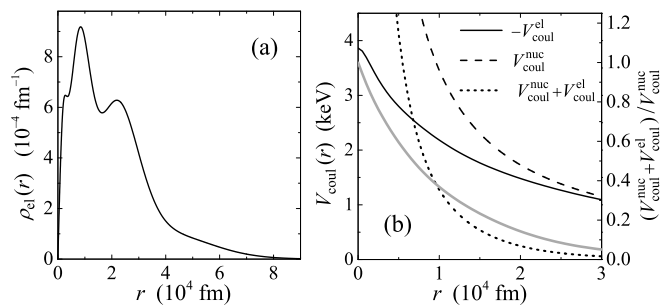


FIG. 18. Panel (a) shows electron density for 24 lowest electron shells in  $^{45}\text{Fe}$  (normalized for integration over  $dr$ ). Left axis of panel (b) shows proton potential for Coulomb interaction of nucleus, electron shell, and their difference (screened potential). The ratio of the screened potential to the nuclear is shown by gray curve opposite the right axis.

Coulomb potential is noticeably reduced due to the screening compared to nuclear Coulomb potential (the reduction factor is 0.8). At 7000 fm the reduction factor is 0.5 and it tends to zero at 30000 fm.

The radial stabilization of the values  $\varepsilon$  and  $\cos(\theta_k)$  in the screening case compared to the purely nuclear case is shown in Fig. 13 for one selected trajectory. It can be seen that in the screening case, the trajectory stabilizes at  $\rho \sim (3 - 4) \times 10^4$  fm. In the purely nuclear case, the minor drift of the trajectory continues to much larger  $\rho$  values. The calculations show that in the “T” system, the screening effect is largest for the variable  $\cos(\theta_k)$ . It is typically at the level of 0.6% of the absolute value of this variable and, for  $\rho_{\text{max}} = 1000$  fm, it typically accounts for 3 – 4% of the CE effect. For an effect which is 0.6% at the absolute scale it is difficult to speculate about its observability just now: its scale is comparable to the widths of the lines in our plots. However, if we think about it as an effect of the atomic surrounding on nuclear decay properties, then such a value can be considered as an impressive one.

It should be noted that the existence of the screening effects is the subject of the experimental technique employed. For example, the  $2p$  decay in  $^{19}\text{Mg}$  was studied in the decay-in-flight experiment Ref. [6]. In this experiment the  $^{19}\text{Mg}$  g.s. was populated by the neutron knockout from the relativistic beam of the completely stripped  $^{20}\text{Mg}$  ions. The resulting  $^{19}\text{Mg}$  is also completely stripped and can hardly pick up any electrons before the decay. Therefore, in spite of a long lifetime ( $T_{1/2} = 4$  ps, which is much longer than typical recombination time), screening in this experiment will have different character, compared to the case discussed above for  $^{45}\text{Fe}$ .

### C. Self-similar solutions

From Figs. 9 and 12, it is possible to see that there exist so called “stationary points” in the kinematical

$\{\varepsilon, \cos(\theta_k)\}$  plane in the “T” system. For such points, the classical trajectories in this plane have zero length. For the degenerate situation  $\varepsilon \equiv 1$ , the stationary behavior is trivial; this situation is not very interesting as the phase space for such configurations in the quantum-mechanical problem tends to zero. However there exist nondegenerate stationary points, and which for two-proton decay with a heavy core  $\{A_3, Z_3\}$  are found as:

$$\varepsilon = \frac{(1 + A_3/2)(Z_3/A_3)^{2/3}}{2A_3 + (Z_3/A_3)^{2/3}}, \quad \cos(\theta_k) = 0. \quad (25)$$

These stationary points are defined by the condition that the force acting on each particle is always directed exactly along the line connecting that particle with the center of mass of the whole three-body system. Such stationary points should exist for any two-body potential with the same power dependence on radius  $V(r) \sim r^n$  for each pair of the particles. The values of  $\varepsilon$  equal to 0.497, 0.382, 0.379 are found for  $^6\text{Be}$ ,  $^{19}\text{Mg}$ , and  $^{45}\text{Fe}$ , respectively, by Eq. (25) as well as by a direct calculations using Eq. (6). It is clear that the solution, which is a stationary one in the  $\{\varepsilon, \cos(\theta_k)\}$  plane, is an analogue of the Lagrange solution in celestial mechanics (with reservation that we are dealing here with repulsive  $1/r$  potentials).

The multi-cluster decays of nuclear systems has been qualitatively studied in Ref. [20]. In this work a quasi-classical approach was used, based on the classical self-similar solutions of the few-body Coulomb problem. The stationary point discussed above represents such a self-similar solution in our specific case. It was concluded in Ref. [20] that “Three-cluster configuration asymptotically approaches to an expanding self-similar triangle whose sides obey the  $(M/Z)^{1/3}$  rule.” This statement is probably not completely correct. It can be seen from Figs. 9 and 12 that there is a trend for classical trajectories to tend somehow towards the stationary point which corresponds to a self-similar solution. This trend leads to certain systematic modifications of the momentum distributions by the long-range Coulomb interaction. However as we have seen in this work, the whole picture is more complex. The total distributions occupy broad regions of the kinematical plane. They are determined mainly by the internal structure of the three-body system and the decay dynamics under the barrier, than by the long-range Coulomb interaction outside of the barrier. Classical trajectories originating on the hypersphere of large radius each converge to its own final position which, in a general case, could have nothing in common with a stationary point.

## VII. CONCLUSION

In this work we discuss the extrapolation along the classical trajectories as a method to improve the momentum distributions for radioactive  $2p$  decay (true three-body decay). The proposed method provides near perfect description of the distributions in the test cases of

simplified three-body Hamiltonians. In the case of real three-body Coulomb interactions considerable quantitative effects on the distributions are observed. In the case of the lightest  $2p$ -emitter  ${}^6\text{Be}$  this effect is minor, but in the heavier  $2p$ -emitters ( ${}^{19}\text{Mg}$  and  ${}^{45}\text{Fe}$ ) the improvement is essential for the precise description of the distributions.

It should be emphasized that some aspects of the momentum distributions for  $2p$  decays are sensitive to the long-range three-body Coulomb interaction, while the others are absolutely insensitive. Namely, the angular distribution in the Jacobi “T” system and the energy distribution in the Jacobi “Y” system are considerably modified by the classical extrapolation. Two other inclusive distributions (the energy distribution in the Jacobi “T” system and the angular distribution in the Jacobi “Y” system) are essentially not influenced by the classical extrapolation. Therefore the long-range part of the three-body Coulomb does not practically change the information about the internal structure of the decaying system which is contained in the latter distributions.

Attention should be paid to the huge range which is required both for the extrapolation range ( $\sim 10^5$  fm) and for the starting point of the classical procedure ( $\sim 10^3$  fm) at typical decay conditions. The classical procedure is applicable only for distances above 500 – 1500 fm (in  $\rho$  variable) for the considered set of  $2p$  emitters (which is actually quite representative). The intermediate distances from 30 – 100 fm (where the protons come from

under the Coulomb barrier) to around 1000 fm should to be treated quantum mechanically to obtain decent results from the classical extrapolation.

We have shown that the electron screening can have a sizable effect on the momentum distribution in the  $2p$  decay of atomic  ${}^{45}\text{Fe}$ . So, the  $2p$  radioactivity belongs to a rare class of nuclear phenomena, which exist on the borderline with atomic phenomena. There exist examples of weak radioactive decay modification induced by atomic electrons (e.g. due to the energy conditions making  $\beta^-$  decay possible only into bound electron states [21] or due to the hyperfine effect [22]). We think that the sizeable sensitivity of the radioactive decay via particle emission due to a modification of the potential barrier properties in the atomic environment is demonstrated in our work for the first time.

## VIII. ACKNOWLEDGMENTS

L.V.G. acknowledges the support from Deutsche Forschungsgemeinschaft grant 436 RUS 113/907/0-1, FAIR-Russia Research Center grant, Russian Foundation for Basic Research grants RFBR 08-02-00892, RFBR 08-02-00089-a, and Russian Ministry of Industry and Science grant NSh-7235.2010.2.

- 
- [1] V. I. Goldansky, Nucl. Phys. **19**, 482 (1960).
  - [2] M. Pfützner, E. Badura, C. Bingham, B. Blank, M. Chartier, H. Geissel, J. Giovannazzo, L. V. Grigorenko, R. Grzywacz, M. Hellstrom, Z. Janas, J. Kurcewicz, A. S. Lalleman, C. Mazzocchi, I. Mukha, G. Munzenberg, C. Plettner, E. Roeckl, K. P. Rykaczewski, K. Schmidt, R. S. Simon, M. Stanoiu, J.-C. Thomas, Eur. Phys. J. A **14**, 279 (2002).
  - [3] J. Giovannazzo, B. Blank, M. Chartier, S. Czajkowski, A. Fleury, M. J. Lopez Jimenez, M. S. Pravikoff, J.-C. Thomas, F. de Oliveira Santos, M. Lewitowicz, V. Maslov, M. Stanoiu, R. Grzywacz, M. Pfützner, C. Borcea, B. A. Brown, Phys. Rev. Lett. **89**, 102501 (2002).
  - [4] L. V. Grigorenko, T. D. Wiser, K. Mercurio, R. J. Charity, R. Shane, L. G. Sobotka, J. M. Elson, A. H. Wuosmaa, A. Banu, M. McCleskey, L. Trache, R. E. Tribble, and M. V. Zhukov, Phys. Rev. C **80**, 034602 (2009).
  - [5] I. Mukha, L. Grigorenko, K. Sümmerer, L. Acosta, M. A. G. Alvarez, E. Casarejos, A. Chatillon, D. Cortina-Gil, J.M. Espino, A. Fomichev, J. E. Garcia-Ramos, H. Geissel, J. Gomez-Camacho, J. Hofmann, O. Kiselev, A. Korshennikov, N. Kurz, Yu. Litvinov, I. Martel, C. Nociforo, W. Ott, M. Pfützner, C. Rodriguez-Tajes, E. Roeckl, M. Stanoiu, H. Weick, and P. J. Woods, Phys. Rev. C **77**, 061303(R) (2008).
  - [6] I. Mukha, K. Sümmerer, L. Acosta, M. A. G. Alvarez, E. Casarejos, A. Chatillon, D. Cortina-Gil, J. Espino, A. Fomichev, J. E. Garcia-Ramos, H. Geissel, J. Gomez-Camacho, L. Grigorenko, J. Hofmann, O. Kiselev, A. Korshennikov, N. Kurz, Yu. Litvinov, I. Martel, C. Nociforo, W. Ott, M. Pfützner, C. Rodriguez-Tajes, E. Roeckl, M. Stanoiu, H. Weick, and P. J. Woods, Phys. Rev. Lett. **99**, 182501 (2007).
  - [7] K. Miernik, W. Dominik, Z. Janas, M. Pfützner, L. Grigorenko, C. R. Bingham, H. Czyrkowski, M. Cwiok, I. G. Darby, R. Dabrowski, T. Ginter, R. Grzywacz, M. Karny, A. Korgul, W. Kusmierz, S. N. Liddick, M. Rajabali, K. Rykaczewski, and A. Stolz, Phys. Rev. Lett. **99**, 192501 (2007).
  - [8] Ivan Mukha, Ernst Roeckl, Leonid Batist, Andrey Blazhev, Joachim Döring, Hubert Grawe, Leonid Grigorenko, Mark Huyse, Zenon Janas, Reinhard Kirchner, Marco La Commara, Chiara Mazzocchi, Sam L. Tabor, Piet Van Duppen, Nature **439**, 298 (2006).
  - [9] L. V. Grigorenko, R. C. Johnson, I. G. Mukha, I. J. Thompson, and M. V. Zhukov, Phys. Rev. Lett. **85**, 22 (2000).
  - [10] L. V. Grigorenko, R. C. Johnson, I. G. Mukha, I. J. Thompson, M. V. Zhukov, Phys. Rev. C **64**, 054002 (2001).
  - [11] L. V. Grigorenko, and M. V. Zhukov, Phys. Rev. C **68**, 054005 (2003).
  - [12] L. V. Grigorenko and M. V. Zhukov, Phys. Rev. C **76**, 014008 (2007).
  - [13] L. V. Grigorenko and M. V. Zhukov, Phys. Rev. C **76**, 014009 (2007).
  - [14] L. V. Grigorenko, I. G. Mukha, I. J. Thompson, and M. V. Zhukov, Phys. Rev. Lett. **88**, 042502 (2002).

- [15] L. V. Grigorenko, I. G. Mukha, and M. V. Zhukov, Nucl. Phys. **A713**, 372 (2003); erratum **A740**, 401 (2004).
- [16] L. V. Grigorenko, I. G. Mukha, and M. V. Zhukov, Nucl. Phys. **A714**, 425 (2003).
- [17] L. V. Grigorenko, T. D. Wiser, K. Miernik, R. J. Charity, M. Pfützner, A. Banu, C. R. Bingham, M. Cwiok, I. G. Darby, W. Dominik, J. M. Elson, T. Ginter, R. Grzywacz, Z. Janas, M. Karny, A. Korgul, S. N. Liddick, K. Mercurio, M. Rajabali, K. Rykaczewski, R. Shane, L. G. Sobotka, A. Stolz, L. Trache, R. E. Tribble, A. H. Wuosmaa, and M. V. Zhukov, Phys. Lett. **B677**, 30 (2009).
- [18] L. Rosenberg, Phys. Rev. D **8**, 1833 (1973).
- [19] S. P. Merkuriev, Theor. Math. Phys. **32**, 680 (1977).
- [20] O. I. Kartavtsev, Few-Body Systems **34**, 39 (2004).
- [21] M. Jung, F. Bosch, K. Beckert, H. Eickhoff, H. Folger, B. Franzke, A. Gruber, P. Kienle, O. Klepper, W. Koenig, C. Kozhuharov, R. Mann, R. Moshhammer, F. Nolden, U. Schaaf, G. Soff, P. Spadtke, M. Steck, Th. Stohlker, K. Sümmerner, Phys. Rev. Lett. **69**, 2164 (1992).
- [22] Yu. A. Litvinov, F. Bosch, H. Geissel, J. Kurcewicz, Z. Patyk, N. Winckler, L. Batist, K. Beckert, D. Boutin, C. Brandau, L. Chen, C. Dimopoulou, B. Fabian, T. Faestermann, A. Fragner, L. Grigorenko, E. Haettner, S. Hess, P. Kienle, R. Knöbel, C. Kozhuharov, S. A. Litvinov, L. Maier, M. Mazzocco, F. Montes, G. Münzenberg, A. Musumarra, C. Nociforo, F. Nolden, M. Pfützner, W. R. Plass, A. Prochazka, R. Reda, R. Reuschl, C. Scheidenberger, M. Steck, T. Stöhlker, S. Torilov, M. Trassinelli, B. Sun, H. Weick, and M. Winkler, Phys. Rev. Lett. **99**, 262501 (2007).